



## Measurement of the charge of airborne 3–10 $\mu\text{m}$ spherical dielectric particles charged in an AC unipolar charger

J.E.J. Dalley\*, R.S. Greenaway, Z. Ulanowski, E. Hesse, P.H. Kaye

*Science and Technology Research Institute, University of Hertfordshire, Hatfield AL10 9AB, UK*

Received 16 February 2005; received in revised form 18 February 2005; accepted 18 February 2005

### Abstract

The charges of airborne 3, 5 and 10  $\mu\text{m}$  spherical dielectric test particles passing through a novel AC unipolar charger have been measured individually. The measurements show the effectiveness of the charger and provide statistics on the particle charges measured. The 3  $\mu\text{m}$  particles were charged to significantly higher values than expected. These log-normally distributed particle charges were found to have an average significantly above the saturation level for dielectric particles. This is most probably because of increased surface conductivity due to sodium and chlorine surface impurities from dried surfactant used for the storage of such particles.

© 2005 Elsevier Ltd. All rights reserved.

*Keywords:* Pauthenier; Saturation; Charge; Particle; PSL; Polystyrene; Masuda; Boxer; Charger; Duke; Scientific; Microspheres; Unipolar; Uni-polar; Surface; Conductivity

### 1. Introduction

The charging of small airborne particles is useful in a wide range of applications where the controlled movement of particles is required. Examples include electrostatic precipitators, drug inhalation, electrostatic coating and particle analysis systems. The charging of aerosols can be achieved by photovoltaic excitation, static electrification, radioactive ionisation and flame charging. Diffusion charging and field charging are also particularly effective methods which require bombardment of the aerosol with unipolar ions. This can be achieved by using corona discharge where air molecules are ionised in the region of a highly charged electrode and are attracted to a grounding electrode. Using DC corona discharge results

\* Corresponding author. Tel.: +44 1707 284 174; fax: +44 1707 284 185.

E-mail address: [j.dalley@herts.ac.uk](mailto:j.dalley@herts.ac.uk) (J.E.J. Dalley).

in small, charged particles being deflected by the electrostatic field and deposited on the grounding electrode. To avoid unwanted particle deposition an AC electric field can be used as demonstrated by Hewitt (1956).

Jaworek, Adamiak, Krupa, and Castle (2001) and Lackowski (2001) of the Institute of Fluid Flow Machinery (IFFM) at the Polish Academy of Sciences have developed a novel alternating electric field charger which has been characterised by Lackowski, Jaworek, and Krupa (2003). This charger is a simple design to fabricate and is much less complex than the Masuda, Washizu, Mizuno and Akutsu (1978) boxer charger which was assessed by Zevenhoven, Wierenga, Scarlett, and Yamamoto (1994). The University of Hertfordshire was provided with a similar charger and custom-made high-voltage power supply by IFFM and its performance was assessed. The results of this assessment are included in this paper and are of interest because of the effectiveness, relative simplicity and, therefore, reduced cost of the IFFM particle charger.

## 2. Charger description

The AC unipolar charger shown in Fig. 1 uses two arrays of sharp needles pointing towards each other across the aerosol flow which is directed along the middle of the charger between two grids. By applying a voltage gradient between one set of needles and the grids (electric field  $\sim 3$  kV/cm) in the first half cycle of an applied AC square wave (100–200 Hz), the ionised air molecules from one needle tip are attracted across the aerosol flow; in the second half cycle the process reverses. Aerosol passing through the charger is highly charged as the particles are bombarded by many cycles of ion flux. When charged, the particles drift across the charger due to the electric field, and as the applied field reverses so does the drift direction. For a square-wave driving voltage the particles, therefore, trace out a zig-zag or W shaped path as shown

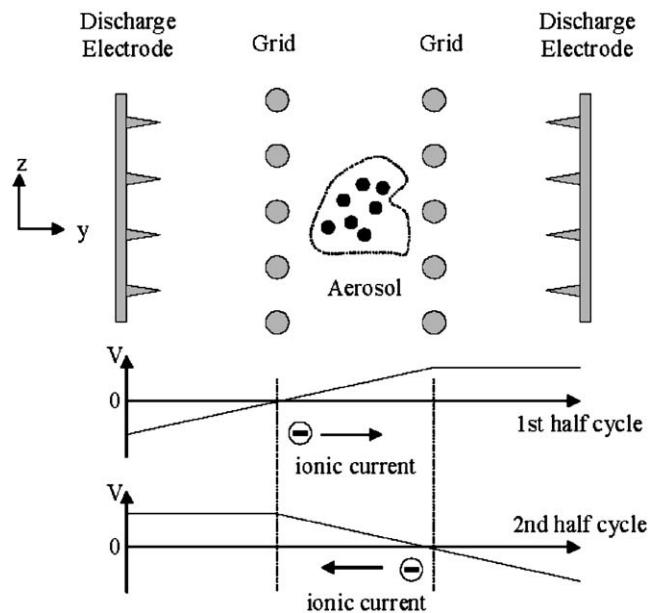


Fig. 1. Schematic diagram of the charger (end view) and the applied voltages.

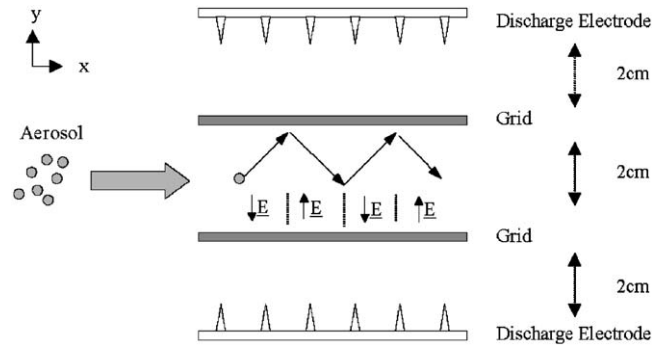


Fig. 2. Schematic diagram (top view) of an aerosol particle passing through the (square wave) AC electric field charger. The particle becomes negatively charged and follows a zig-zag path as the applied electric field causes the transverse drift velocity to alternate.

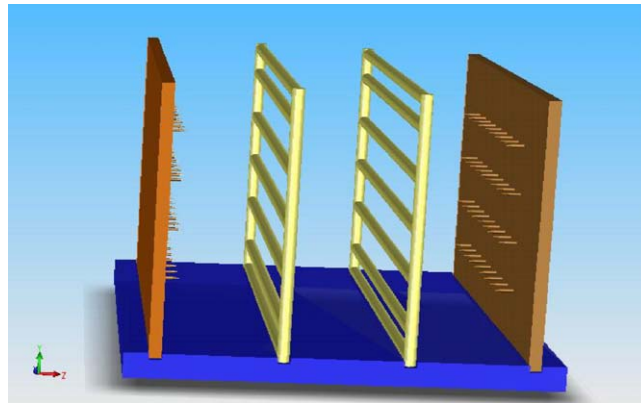


Fig. 3. Picture of the particle charger showing the outer discharge electrodes and the inner grids. The aerosol is drawn through the charging region between the two grids.

in Fig. 2. For clarity, a CAD drawing of the charger is presented in Fig. 3 showing the inner grids and the 4 rows of needles on each discharge electrode. The 3 mm long needles have a 5 mm horizontal and 8 mm vertical spacing and are mounted on ( $2 \times 43 \times 73$  mm) brass plates. The grids are fabricated from steel rod with a diameter of 2 mm. The central five bars of each grid have an 8 mm vertical spacing allowing an unobstructed path for the ions from the discharge electrodes. As shown in Fig. 2, the spacing between the 4 components is 20 mm making the overall volume of the charger approximately  $60 \times 43 \times 73$  mm.

### 3. Charging theory

The theory of particle charging in an electric field by unipolar ions is relatively well known (Pauthenier & Moreau-Hanot, 1932; Lawless, 1996). Field charging theory is adequate for large particles and high fields while diffusion charging theory is used for small particles or low fields. The saturation charge due

to field charging is known in some literature as the Pauthenier limit (Zevenhoven, 1999; Lackowski et al., 2003) and is given for either conducting or dielectric spheres of radius  $r$  in electric field  $E$  by the following expressions:

Conducting spherical particle saturation charge

$$q_s = 12\pi\epsilon_0 r^2 E. \quad (1)$$

Dielectric spherical particle saturation charge

$$q_s = 12\pi\epsilon_0 r^2 E \frac{\epsilon_r}{\epsilon_r + 2}, \quad (2)$$

where  $\epsilon_0$  is the permittivity of free space. The diffusion charge can be calculated approximately using the following equation from Hinds (1999) for the number of diffusion charges acquired in time  $t$ ,  $n(t)$ .

$$n(t) = \frac{d_p k T}{2K_E e^2} \ln \left[ 1 + \frac{\pi K_E d_p \bar{c}_i e^2 N_i t}{2kT} \right], \quad (3)$$

where  $d_p$  is the particle diameter,  $\bar{c}_i$  the mean thermal speed of air ions (240 m/s),  $N_i$  the concentration of air ions (typically  $\sim 10^{13}$  for corona chargers),  $K_E = 1/4\pi\epsilon_0 = 9.0 \times 10^9$ ,  $k$  the Boltzmann's constant,  $T$  the absolute temperature and  $e$  the electronic charge.

For  $N_i t > 10^{13}$  s/m<sup>3</sup>, Hinds (1999) states that this is accurate to a factor of 2 for particles with diameter 0.05 to 40  $\mu\text{m}$ . A more accurate but less convenient expression is given by Lawless (1999). This requires numerical integration and since a precise calculation of the diffusion charge is not required in this paper, the simple expression from Hinds has been used.

In some circumstances both field and diffusion charging occur at the same time. This is known as continuum charging (Lawless, 1996; Hinds, 1999) where particle charge is the sum of the contributions from field and diffusion charging.

#### 4. Experiment design

Using a 660 nm diode laser and cylindrical lens, a horizontal light sheet ( $xy$  plane in Fig. 4) was generated to illuminate individual particles as they passed through the charger. The movement of these particles was observed by a digital camera positioned above the centre of the charger pointing vertically downwards with the focal plane of the camera coincident with the light sheet. The camera exposure time of about 100 ms enabled the oscillatory path of illuminated particles to be traced out on a single image (Figs. 5 and 6). Particles near the inlet duct were drawn through the charger by a pump operating at 201  $\text{min}^{-1}$  which gave a typical particle velocity of 0.15 m/s. It should be noted that if no air flow is present to draw the particles through the charger rapidly they are simply ejected out of the charging region.

To be able to make comparable charge measurements for a 4–7 kV amplitude range, the frequency selection of the AC driving voltage was limited by the size of the charging region for high amplitudes and the resolution of the camera for low amplitudes. This resulted in a narrow frequency range of 100–200 Hz, so measurements were made at 100 and 200 Hz.

The test particles used were 4000 series Polymer Microsphere Size Standards from Duke Scientific Corp., Palo Alto, CA, USA. The NIST traceable mean diameter of these polystyrene microspheres,

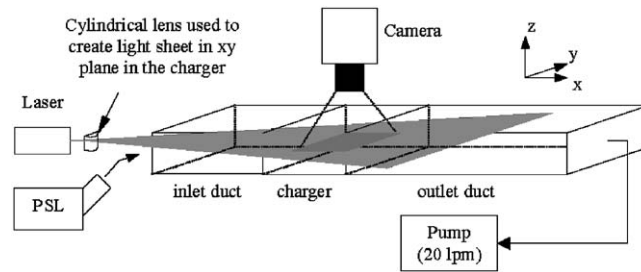


Fig. 4. Schematic diagram of the experiment showing the particles (polystyrene microspheres) being sucked into the inlet duct where they are illuminated by a light sheet and then imaged by a camera above the charging region.

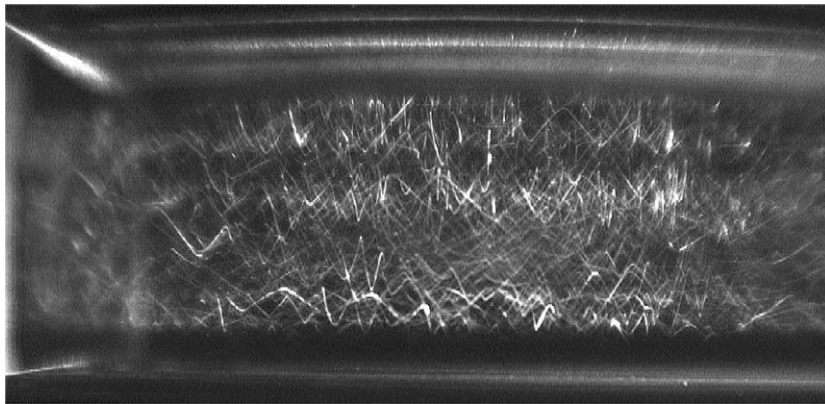


Fig. 5. Image of  $10\ \mu\text{m}$  alumina particles (probably aggregates as well as single particles) drawn from left to right through the charging region which is subject to a square-wave AC electric field of  $3\ \text{kV}/\text{cm}$ .

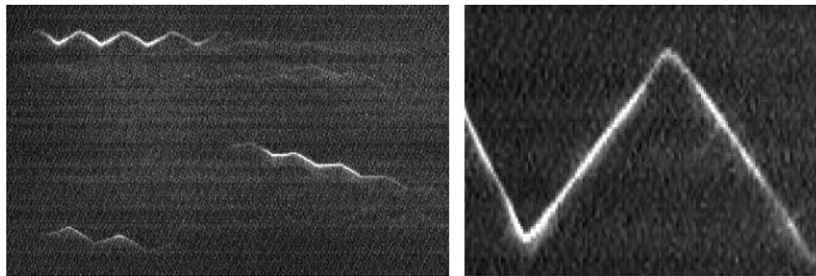


Fig. 6. Characteristic triangular waveforms of charged particles in the charger.

commonly called PSL, have a certified uncertainty of less than  $\pm 1\%$  measured by optical microscopy. The relative dielectric constant of polystyrene is 2.5. These microspheres were chosen to avoid potentially biasing results with unwanted size variations as had been seen with previous test measurements with alumina and silica. The square wave AC voltage was used since this provided a constant voltage in each

half cycle and a sharp transition between voltage cycles. The particles were launched using a variety of methods: 3  $\mu\text{m}$  particles were launched using a TSI Tri-jet Aerosol Generator (TSI Inc., St. Paul, MN, USA). The 5 and 10  $\mu\text{m}$  PSL were launched using a nebuliser driven by compressed air and passed through a drying column. The dilute PSL suspension used for the Tri-jet and nebuliser was typically 0.5–1 ml (10–20 drops) of the manufacturers PSL concentrated suspension (solid contents were 0.5% for 3  $\mu\text{m}$  and 0.3% for the 5 and 10  $\mu\text{m}$  particles) mixed with 40 ml of filtered distilled water. The ease of launching 3  $\mu\text{m}$  PSL made it the predominant source of measurement data.

## 5. Sample images

Fig. 5 shows a large number of alumina particles being charged as they drift through the charger. Reducing the particle concentration of the PSL analysed in this work and zooming into a small region in the middle of the charger yields a clearer picture, as in Fig. 6. The recorded images were enhanced from the original by photo-editing software. The pixel coordinates of the maxima and minima of the trajectory waveforms were manually identified and converted to distance coordinates with the aid of a reference image of a calibrated scale. From the images two things are immediately obvious: the clean straight lines of the triangular oscillations and the sharp V-shaped transitions between the different phases of the AC electric field. Another feature of the particle traces shown in Fig. 6 is the apparently uniform amplitude of the illuminated oscillations captured in a single image. The traces were not always axial and so the charge was calculated using the method outlined in the next section.

## 6. Data interpretation

A particle of charge  $q$  in an electric field  $E$  is subject to an electrostatic force,  $F = qE$ . This force will cause the particle to accelerate until the viscous drag of the air, described by Stoke's equation (Hinds, 1999), increases and a steady-state drift velocity in the electric field is reached where the two forces balance. At such a point for spherical particles:

$$F_{\text{electrostatic}} = qE = F_{\text{drag}} = 3\pi\eta d v_{\text{drift}}, \quad (4)$$

where  $\eta$  is the gas viscosity,  $d$  is the particle diameter and  $v_{\text{drift}}$  is the drift velocity, which is parallel with the  $y$ -axis in this experiment. Note that the Cunningham correction factor is neglected here as it is only significant for particles less than 1  $\mu\text{m}$ . So in a known electric field, the unknown charge on a particle can be found by measuring the drift velocity  $v_{\text{drift}}$  and using the following equation for the unknown particle charge:

$$q = \frac{3\pi\eta d v_{\text{drift}}}{E}. \quad (5)$$

This equation is valid only for spherical particles.

As can be seen in Fig. 6, the particle's mean trajectory (about which it oscillates in the electric field) is typically not parallel with the centre line of the charger ( $x$ -axis) as would normally be expected for lamina flow. This effect is primarily due to the charging of the particle which gives differing drift velocities during the two half periods of the AC oscillation (Zevenhoven et al., 1994). The charging region was

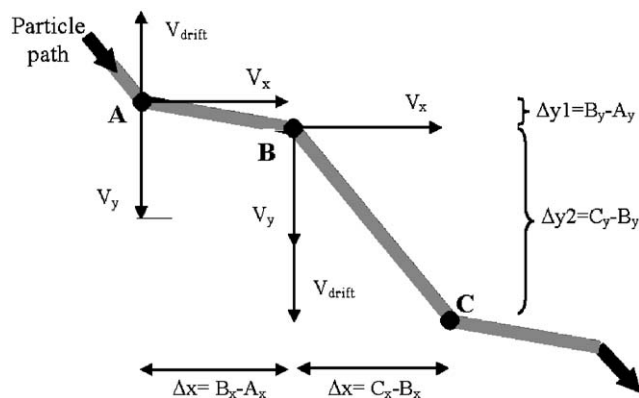


Fig. 7. Section of a measured particle trajectory ABC showing the different y-axis displacements that result from the vector sum of the particle's own velocity ( $v_x + v_y$ ) and the alternating drift velocity ( $v_{drift}$ ) resulting from the applied electric field.

approximately 50 mm long, 20 mm wide and 40 mm high ( $x$ -,  $y$ - and  $z$ -axis, respectively). The field of view of the camera in the  $xz$  plane was approximately 13 mm  $\times$  9 mm in the centre of the charger. The rapid charging of the particles (Jaworek & Krupa, 1989) as particles enter the charger results in a relatively slow charging rate when the particles come into the field of view of the camera. The particle is drawn through  $\sim 19$  mm of the charger before it comes into the field of view of the camera for 13 mm and then carries on being charged for a further  $\sim 19$  mm before exiting the charger. An analysis of some well-illuminated long (3  $\mu$ m) particle traces showed that the charging rate is approximately 0.5–3% per half cycle at 100 Hz. The particle would have been subject to  $\sim 17$ –100 Hz AC cycles of charging before this point. This explains the apparently uniform amplitude and lack of curvature of the oscillations which are normally only illuminated for a couple of cycles. The relatively low-charging rate in the field of view of the camera meant that for a single AC cycle, the particle charge and therefore the drift velocity could be assumed to be approximately constant (to within 6%). This is an acceptable accuracy given that the result is a snapshot of the particle charge near the middle of the charger.

Particles drawn through the charger have a constant velocity along the  $x$ -axis,  $v_x$ . If in passing through the charger they acquire a velocity component along the  $y$ -axis,  $v_y$ , in addition to the drift velocity,  $v_{drift}$  the particle will oscillate along a non-axial vector. The vector sum of  $v_x$ ,  $v_y$  and  $v_{drift}$  then gives rise to asymmetric oscillations as shown in Fig. 7. Subtracting the two displacements along the  $y$ -axis removes the contribution from the  $v_y$  component and so the following equation can be used to determine the drift velocity:

$$v_{drift} = \frac{\Delta y_2 - \Delta y_1}{T_{sq}}, \quad (6)$$

where  $T_{sq}$  is the period of the (square wave) driving voltage. Therefore, the co-ordinates of three vertices (marked as black diamonds in Fig. 7) on a particle trajectory are all that are required to quantify  $v_{drift}$ .

Table 1  
Pauthenier (field) charge limit for 3 μm spherical PSL particles as a function of applied AC electric field

	4 kV driving voltage $E = 2 \text{ kV/cm}$	5 kV driving voltage $E = 2.5 \text{ kV/cm}$	6 kV driving voltage $E = 3 \text{ kV/cm}$	7 kV driving voltage $E = 3.5 \text{ kV/cm}$
Dielectric particle ( $\epsilon_r = 2.5$ )	$0.8\text{E} - 16 \text{ C}$ (499e)	$1.0\text{E} - 16 \text{ C}$ (624e)	$1.3\text{E} - 16 \text{ C}$ (811e)	$1.5\text{E} - 16 \text{ C}$ (936e)
Conducting particle	$1.5\text{E} - 16 \text{ C}$ (936e)	$1.9\text{E} - 16 \text{ C}$ (1186e)	$2.3\text{E} - 16 \text{ C}$ (1436e)	$2.6\text{E} - 16 \text{ C}$ (1623e)

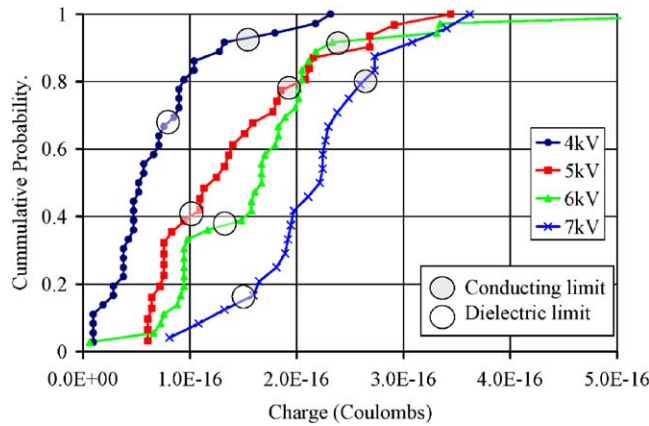


Fig. 8. Measured charge distribution for 3 μm PSL for 100 Hz square-wave AC voltage amplitudes of 4, 5, 6 and 7 kV.

### 7. Statistical results

The measured charge distributions were found to be log-normal in common with other measurements of this type (Frank, Cederfelt, & Martinsson, 2004; Kirsh & Zagnit’ko, 1988). Table 1 presents the saturation charges predicted by the Pauthenier limit as a function of the electric field strength used in the experiment. Figs. 8 and 9 show the CDFs (cumulative density functions) of measured charges for 3 μm PSL at 100 and 200 Hz for square wave driving voltages of 4–7 kV. The saturation charges for both dielectric and conducting particles are also plotted for comparison. To enable comparison with the substantial work of Kirsh and Zagnit’ko (1988), where measurements of almost 15,000 particles were made, results for the average of the log-normally distributed data are presented. With the exception of the 4 kV measurements, the average of the measured charges was always above the saturation charge predicted for the dielectric particle.

The minimum resolvable charge for the 100 Hz measurements was approximately  $0.1 \times 10^{-16} \text{ C}$ , whilst for 200 Hz this increased to  $0.2 \times 10^{-16} \text{ C}$ . Results at or below this level were recorded to enable the CDFs to be generated. In the measurements at 4 kV where this was an issue there was a small bias on the average but a large bias on the standard deviation especially the 4 kV results at 200 Hz.

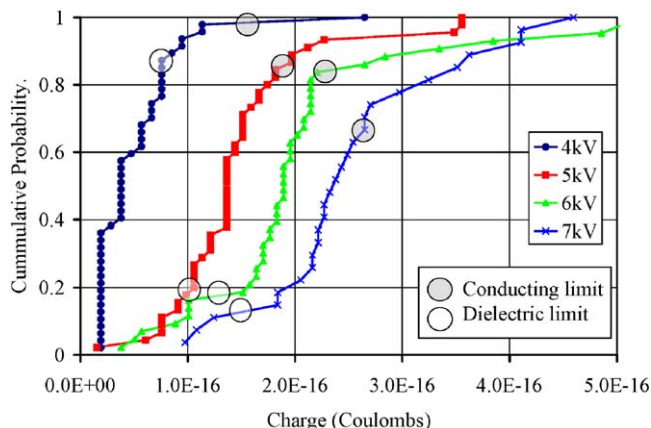


Fig. 9. Measured charge distribution for 3  $\mu\text{m}$  PSL for 200 Hz square-wave AC voltage amplitudes of 4, 5, 6 and 7 kV.

Table 2  
Average and standard deviation of measured charge data

	Number of unfiltered data points	Average (e)	Average (C)	$\sigma$	Number of filtered data points	Average (e)	Average (C)	$\sigma$
100 Hz 4 kV	36	312	$0.5\text{E} - 16$	2.3	28	375	$0.6\text{E} - 16$	1.6
100 Hz 5 kV	31	749	$1.2\text{E} - 16$	1.7	30	749	$1.2\text{E} - 16$	1.7
100 Hz 6 kV	36	874	$1.4\text{E} - 16$	2.0	34	936	$1.5\text{E} - 16$	1.5
100 Hz 7 kV	24	1311	$2.1\text{E} - 16$	1.4	24	1311	$2.1\text{E} - 16$	1.4
200 Hz 4 kV	47	250	$0.4\text{E} - 16$	2.8	44	250	$0.4\text{E} - 16$	2.3
200 Hz 5 kV	45	811	$1.3\text{E} - 16$	1.7	44	874	$1.4\text{E} - 16$	1.5
200 Hz 6 kV	43	1124	$1.8\text{E} - 16$	1.7	38	1186	$1.9\text{E} - 16$	1.4
200 Hz 7 kV	27	1498	$2.4\text{E} - 16$	1.4	27	1498	$2.4\text{E} - 16$	1.4

The significant errors in estimating the charge arise from two sources:

1. the systematic error when estimating the pixels/cm from the image of the distance calibration grid placed in the charger before each test,
2. the random error from estimating the pixel co-ordinates of the zig-zag maxima and minima. This depended on the quality and sharpness of focus of the image.

The sum of these errors was typically  $0.1 \times 10^{-16}$ – $0.2 \times 10^{-16}$  C with a maximum error of  $0.4 \times 10^{-16}$  C. Error bars have not been plotted on the graphs to aid clarity. The average and standard deviation for each measurement is shown in Table 2. The effect of filtering out some of the outlying data points is also shown where the typical standard deviation is in the range of 1.4–1.7. The standard deviation of 2.3 for the 4 kV 200 Hz measurement is not representative because of the minimum resolvable charge issue.

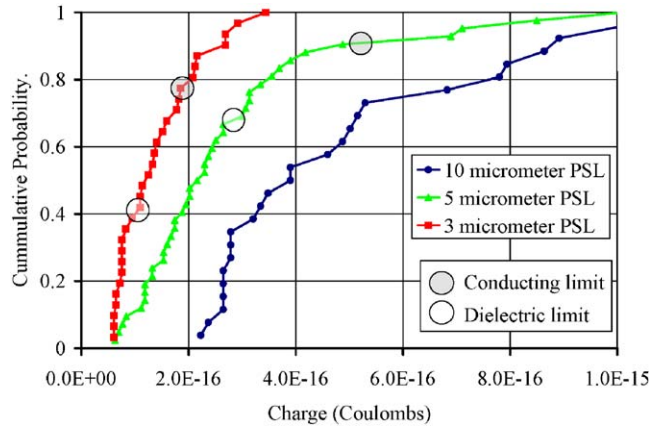


Fig. 10. Measured charge for 3, 5 and 10  $\mu\text{m}$  PSL under the same conditions (5 kV, 100 Hz).

Table 3

Charger efficiency based on Pauthenier charge limit for dielectric and conducting particle assumptions

5 kV 100 Hz ( $\mu\text{m}$ )	Number of unfiltered data points	Average (e)	Average (C)	$\sigma$	Conducting particle charge limit (e)	Conducting particle charge limit (C)	Charger efficiency (conductor) (%)	Charger efficiency (dielectric) (%)
3	31	749	$1.2\text{E}-16$	1.7	1186	$1.9\text{E}-16$	76	118
5	42	1373	$2.2\text{E}-16$	1.9	3246	$5.2\text{E}-16$	43	77
10	26	2747	$4.4\text{E}-16$	1.7	13109	$2.1\text{E}-15$	21	38

Measurements were also made with 5 and 10  $\mu\text{m}$  PSL and are presented in Fig. 10. The average of the measured charges for both 5 and 10  $\mu\text{m}$  were below the Pauthenier charge limit for dielectric particles as can be seen in Table 3.

## 8. Analysis

In terms of the Pauthenier limit for dielectric particles the charger efficiency for 3  $\mu\text{m}$  PSL is typically over 100% with a maximum of 163%. Assuming that the particle is a perfect conductor, the maximum charger efficiency is 97%. These results can be seen in Tables 4 and 5. This slight increase in the charger efficiency as a function of frequency can be explained by a slightly increased ionic charging current (Lackowski et al., 2003). In the same paper, the space charge density for this type of charger was also measured and correcting for the different grid separations and voltages a space charge density of  $6 \mu\text{C m}^{-3}$  is expected for an electric field of  $2.5 \text{ kV cm}^{-1}$  (driving voltage of 5 kV) which is equivalent to an ion concentration,  $N_i = 3.8 \times 10^{13} \text{ m}^{-3}$  and is in common with the  $> 10^{13} \text{ m}^{-3}$  concentrations expected for corona chargers (Hinds, 1999, p. 327). Lackowski (2003) notes that not all of the air ions travel through the

Table 4  
Charger efficiency for different driving voltages at 100 Hz

Driving voltage (kV)	Electric field (kv/cm)	Dielectric particle charge limit (e)	Dielectric particle charge limit (C)	Charger efficiency (dielectric) (%)	Conducting particle charge limit (e)	Conducting particle charge limit (C)	Charger efficiency (conductor) (%)
4	2	524	8.4E–17	63	936	1.5E–16	47
5	2.5	624	1.0E–16	118	1186	1.9E–16	76
6	3	811	1.3E–16	112	1436	2.3E–16	75
7	3.5	936	1.5E–16	141	1623	2.6E–16	83

Table 5  
Charger efficiency for different driving voltages at 200 Hz

Driving voltage (kV)	Electric field (kv/cm)	Dielectric particle charge limit	Dielectric particle charge limit (C)	Charger efficiency (dielectric) (%)	Conducting particle charge limit (e)	Conducting particle charge limit (C)	Charger efficiency (conductor) (%)
4	2	524	8.4E–17	47	936	1.5E–16	34
5	2.5	624	1.0E–16	127	1186	1.9E–16	79
6	3	811	1.3E–16	144	1436	2.3E–16	91
7	3.5	936	1.5E–16	163	1623	2.6E–16	97

Table 6  
Charge of particles from diffusion charging

Particle size ( $\mu\text{m}$ )	Number of charges	Charge (C)	Percentage of measured charge at 5 kV 100 Hz (%)
3	112	1.8E–17	15
5	206	3.3E–17	15
10	474	7.6E–17	17

charging region and that an efficiency factor of  $\sim 0.6$  should be used which brings the ion concentration  $N_i$  down to  $\sim 2.3 \times 10^{13}$ .

The contribution of diffusion charging has also been estimated. The particles had a mean velocity of  $0.15 \text{ ms}^{-1}$  through the charger ( $x$ -axis) which had an active charging region (along the  $x$ -axis) of 6 cm. As the camera field of view coincided with the centre of the charger, the transit time to this point was 0.2 s. The number of ions passing through the charger for a charging time,  $t$  was  $N_i t$ . For the 0.2 s of charging time, before the particle trajectory was imaged,  $N_i t \sim 0.5 \times 10^{13}$ , i.e. just below the  $N_i t > 10^{13}$  where the diffusion charge formula is accurate to a factor of 2. Hinds also states that the diffusion charge formula is accurate to a factor of 2 for  $N_i t > 10^{12}$  for particles in the range 0.07–1.5  $\mu\text{m}$ , so the formula is used here only to give an indication of the effect of diffusion charging. Table 6 presents these results for the

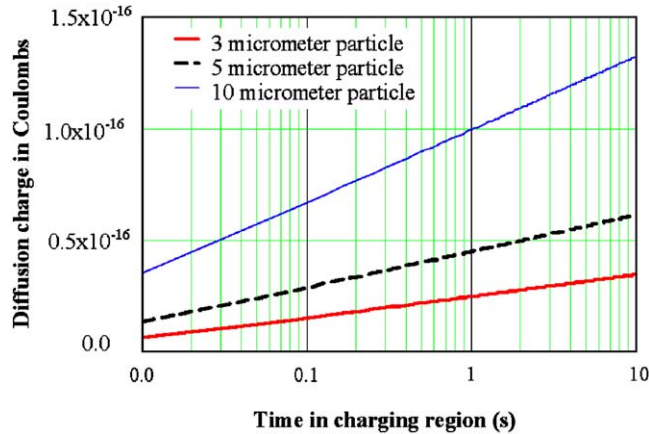


Fig. 11. Estimated diffusion charge in Coulombs as a function of time in the charger using the Hinds (1999) formula for  $n(t)$ .

different sized PSL under the same measurement conditions with an applied driving voltage amplitude of 5 kV at 100 Hz. Note that the charger is most efficient at 200 Hz and 7 kV where the contribution from diffusion charging would only be  $\sim 7\%$ .

The contribution from diffusion charging is, therefore, relatively low and does not explain the high charges measured. The benefit of field charging over diffusion charging for micrometre-sized particles is shown in Fig. 11, where the charging time must increase logarithmically to maintain a linear increase in charge. As a very crude figure for a 3  $\mu\text{m}$  particle assuming the same ion concentration,  $N_i$ , the time required for diffusion charging to match the charge measured from 0.2 s of field charging would be  $\sim 10^9$  s.

A potential explanation for the high level of saturation charge could come from the surfactant used to store the PSL in suspension in its bottle. Using an electron microscope, energy dispersive X-ray (EDX) analysis was used to investigate the elemental composition of PSL with and without surfactant. The PSL particles were stored in suspension in the manufacturer's proprietary solution of water, surfactant and preservative. An 'unwashed PSL' sample was made using a drop of this suspension straight from the storage bottle, dried with compressed air. To create a 'washed PSL' sample, PSL suspension was diluted by a factor of  $10^{12}$  using a centrifuge to sediment out the PSL combined with repeated removal and re-dilution of the suspending phase. As with the other sample, a drop of the washed PSL sediment was dried with compressed air. Both samples required an evaporated gold coating over the sample to prevent charging effects that would distort the electric fields in the electron microscope.

As can be seen in Fig. 12, the 3  $\mu\text{m}$  PSL have a very uniform size, forming even lattice structures. Fig. 13 shows the EDX spectra for both washed and unwashed individual PSL microspheres. The chemical formula for polystyrene is  $(\text{C}_8\text{H}_8)_x$  and the washed PSL shows the expected EDX spectrum with the large carbon peak as well as the peak at 2.1 keV from the gold coating. The spectrum for the unwashed PSL shows the presence of sodium and oxygen. While the electron beam is only  $\sim 10$  nm wide, the reaction volume is not confined to the surface of the PSL but extends into it forming an onion shape below the surface of the order of single cubic micrometers. As Fig. 14 shows, a few of the unwashed PSL showed dried surfactant crystals which gave the opportunity to provide a clearer indication of the surface coating. Focussing the electron beam at the centre of the particle (position A in Fig. 14) resulted in the EDX

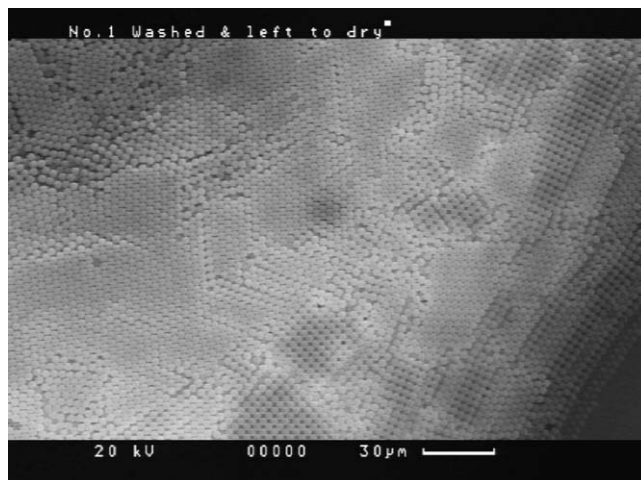


Fig. 12. Stacked layers of 3  $\mu\text{m}$  washed PSL showing the lattice structures resulting from uniformly sized spherical particles.

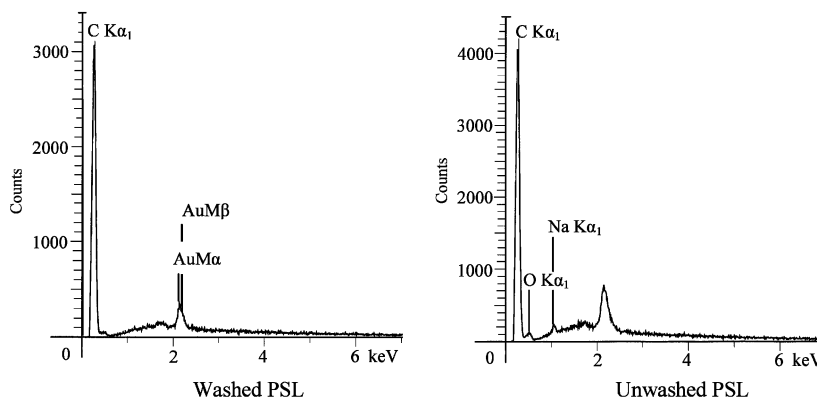


Fig. 13. EDX spectra for washed and unwashed PSL showing the expected carbon peak from the polystyrene particle, the gold sample coating and traces of oxygen and sodium on the unwashed PSL.

spectrum shown in Fig. 15 with the small sodium and oxygen peaks. Moving the electron beam to the crystal (position B in Fig. 14) resulted in a chlorine peak and a sharp increase in the sodium peak. The remaining strong carbon peak results from the reaction volume of the electron beam extending beyond the small crystal and into the PSL. Since Duke Scientific Corp. were unable to account for the presence of the chlorine it may be presumptive to label the crystal as sodium chloride but an analysis of an isolated crystal from the same sample, shown in Fig. 16, clearly identifies strong sodium and chlorine components accounting for 93% of the crystals weight. However, the presence of both sodium and chlorine impurities on the surface of the PSL does provide a plausible explanation for increased surface conductivity.

Another (untested) potential explanation for surface conductivity could come from the surfactant molecule which has a hydrophilic head end and a long tail with a hydrophobic end. When the particle is nebulised the hydrophobic ends attach to the particle and as the inclusion dries, a hydrophilic

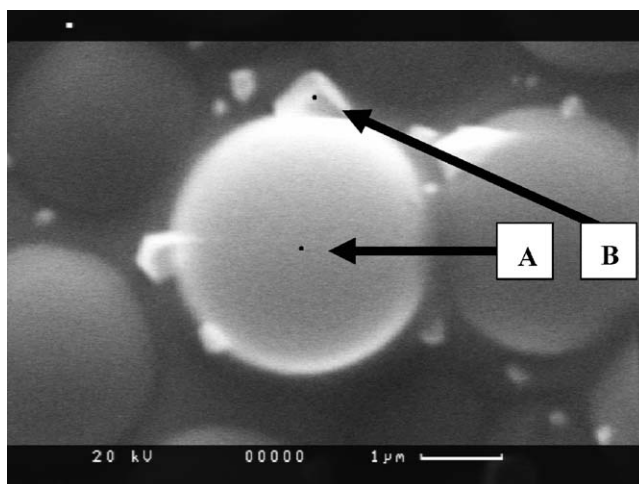


Fig. 14. Location of the  $\sim 10$  nm diameter electron beam used to analyse the elemental composition of the individual PSL particle and the attached crystal.

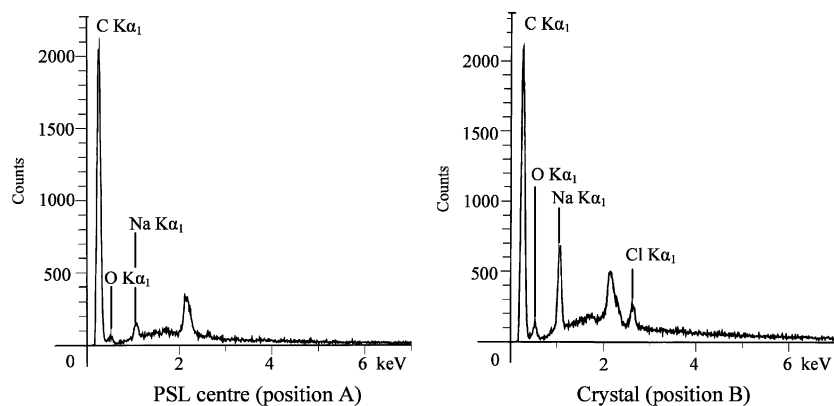


Fig. 15. EDX spectra of an individual unwashed PSL particle and the attached crystal.

coating is formed around the dry particle. The hydrophile is ended by a hydroxide (OH) group and it is the electro-negative hydrogen atom having a loosely bound electron that enables electrical conductivity.

The presence of surface impurities likely to affect the surface conductivity means that the relatively high charge levels for  $3\ \mu\text{m}$  particles could simply be because the charging time (before the particle was imaged) was not long enough for the  $5$  and  $10\ \mu\text{m}$  particles to reach the same level of charge saturation.

The charging of dielectric particles close to the conducting saturation limit has been mentioned, albeit briefly, by Kirsh and Zagnit'ko (1988) and Lawless (1996). These are useful and important papers but given the lack of information on this topic for solid particles, it is hoped that the results presented here will prompt further discussion of this area.

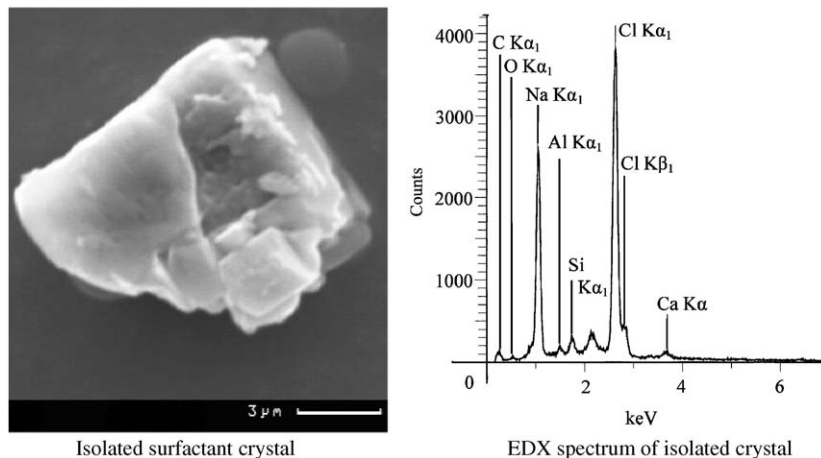


Fig. 16. EDX spectrum of an isolated surfactant crystal (part of the unwashed PSL sample).

## 9. Conclusion

The initial aim of this work was to assess the efficiency of the AC unipolar charger in terms of the Pauthenier limit. Overall, the AC unipolar charger was very effective enabling solid PSL particles to be much more highly charged than could be achieved by diffusion charging. The charging time of 0.2 s (or less) is also much better than could be achieved with a diffusion charger. These attributes are potentially important for applications such as air filtration and removing airborne nanoparticles.

For 5 and 10  $\mu\text{m}$  PSL spheres the average charging efficiency was found to be 77% and 38% of the expected saturation charge for dielectric spherical particles. The charge data was log-normally distributed with a standard deviation of approximately 1.8. For these tests a nebuliser followed by a drying column was used as the particle launch mechanism.

For 3  $\mu\text{m}$  PSL the measured efficiencies have been tabulated for a range of electric fields for 100 and 200 Hz and the standard deviation was typically in the range of 1.4–1.7. The average charging efficiency was found to be significantly above the Pauthenier limit for dielectric particles but still below that of a conductor. This finding has been very briefly noted in previously published aerosol measurements (Pauthenier & Moreau-Hanot, 1932; Kirsh & Zagnit'ko, 1988; Lawless, 1996) but is not widely known and is not well understood. While small particles could be subject to diffusion charging, this effect is not thought to be significant in this case (Hinds, 1999). This is confirmed by charging efficiency measurements showing increasing efficiency with increasing applied electric field. The surfactant used to store the PSL in suspension could, when dried onto the surface of the particle, provide the mechanism for a conductive surface and hence charging efficiency. Using an electron microscope, energy dispersive X-ray (EDX) analysis of the PSL has proved the presence of sodium and chlorine impurities resulting from the surfactant solution. While the microspheres from Duke Scientific Corp. are of very high quality and are useful products for use in aerosol science, the presence of these impurities, and so the potential for increased surface conductivity, should be considered even when the PSL suspension has been diluted significantly.

## References

- Frank, G. P., Cederfelt, S. I., & Martinsson, B. G. (2004). Characterisation of a unipolar charger for droplet aerosols of 0.1–20  $\mu\text{m}$  in diameter. *Journal of Aerosol Science*, 35, 117–134.
- Hewitt, G. W. (1956). The charging of small particles for electrostatic precipitation. *Transactions of the AIEE*, 76, 300.
- Hinds, W. C. (1999). *Aerosol technology*. (2nd ed.), New York: Wiley–Interscience.
- Jaworek, A., & Krupa, A. (1989). Airborne particle charging by unipolar ions in an AC electric field. *Journal of Aerosol Science*, 23, 361–370.
- Jaworek, A., Adamiak, K., Krupa, A., & Castle, G. S. P. (2001). Trajectories of charged aerosol particles near a spherical collector. *Journal of Aerosol Science*, 51, 603–609.
- Kirsh, A. A., & Zagnit'ko, A. V. (1988). Impact charging of small aerosol particles by unipolar ions. *Colloid Journal of the USSR*, 50(5), 731–738.
- Lackowski, M. (2001). Unipolar charging of aerosol particles in alternating electric field. *Journal of Aerosol Science*, 51, 225–231.
- Lackowski, M., Jaworek, A., & Krupa, A. (2003). Current–voltage characteristics of alternating electric field charger. *Journal of Electrostatics*, 58, 77–89.
- Lawless, P. A. (1996). Particle charging bounds, symmetry relations and an analytic charging model for the continuum regime. *Journal of Aerosol Science*, 27, 191–215.
- Masuda, S., Washizu, M., Mizuno, A., & Akutsu, K. (1978). Boxer charger—a novel charging device for high resistivity powders. *Conference Record of the IEEE/IAS Annual Meeting*, 1B, 16–22.
- Pauthenier, M., & Moreau-Hanot, M. (1932). La charge des particules sphériques dans un champ ionise. *Journal de Physique et la Radium*, 3, 590–613 (in French).
- Zevehoven, C. A. P. (1999). Uni-polar field charging of particles: Effects of particle conductivity and rotation. *Journal of Electrostatics*, 46, 1–12.
- Zevehoven, C. A. P., Wierenga, R. D. J., Scarlett, B., & Yamamoto, H. (1994). An evaluation of the Masuda boxer charger. *Journal of Electrostatics*, 32, 133–135.